

ARTICLE OPEN



Corrosion performance and degradation mechanism of a bi-metallic aluminum structure processed by wire-arc additive manufacturing

Amin S. Azar¹✉, Angeliki Lekatou², Martin F. Sunding¹, Joachim S. Graff¹, Nicky Tzima² and Spyros Diplas¹

An Al-5Mg alloy (AA5083) block, deposited over an AA6061 substrate by wire-arc additive manufacturing, was electrochemically tested along two different cross-sectional planes by cyclic polarization in 3.5 wt.% NaCl. The deposited layers and the interlayer boundaries showed similar polarization behavior regardless of the cross-sectional direction. The corrosion of both the substrate and the deposited layers was mainly attributed to the presence of relatively coarse intermetallic Al(Fe, Mn)Si particles. In the substrate, corrosion was governed by deep crevices along the interfaces of directionally aligned Al(Fe, Mn)Si particles with the Al matrix. The deposited layers and the interlayer boundaries showed pitting around numerous Al(Fe, Mn)Si particles and/or Al(Fe, Mn, Cr, Ti)Si at the interlayer boundaries, which were much finer compared to those of the substrate. The abundance of the fine precipitates and their intergranular location caused surface material removal, which was more extensive along the interlayer boundaries. The perpendicular *z-y* and *z-x* planes of the deposited block did not show significant differences in anodic polarization behavior. Differences were more distinct in the case of cathodic polarization. Some anisotropy in polarization behavior was noted through the thickness of the *z-y* plane that complies with the obtained tensile behavior.

npj Materials Degradation (2021)5:26; <https://doi.org/10.1038/s41529-021-00175-4>

INTRODUCTION

Wire-arc additive manufacturing (WAAM) of metallic materials is a method for processing multi-material components. The compositional variation in the deposited layers may potentially influence the corrosion performance of the final component. In addition to composition, the microstructure also varies along the build direction since each deposited layer generates a heat affected zone on the material underneath. This can result in precipitation of secondary phases or local coarsening of the microstructure that will also influence the corrosion properties of the material.

Multi-material constructions with variable properties along a given length scale are good candidates for satisfying advanced design requirements. It was demonstrated that additive manufacturing can produce such components for primary applications such as thermal barriers¹, corrosion protection², wear resistance³, optimization of strength and ductility⁴, and several other opportunities yet to be explored.

Apart from processability and manufacturability challenges, multi-material components may suffer from environmental degradation and corrosion triggered by their dissimilar compositions. It is well known that use of bulk structures consisting of alloys with very different galvanic corrosion potentials may be detrimental for several industrial applications⁵. In this context, the processed multi-materials can be classified into two different groups from a design perspective:

1. Layered components that are designed for applications aiming to protect an underlying material/component when the whole structure is exposed to a degrading environment⁶. Such multi-material components are shaping the vast majority of the recent developments in the field and many researchers reported functionally graded materials (FGM) that prevent or decelerate degradation. Typical

examples include (but are not limited to) thermal barrier coatings (TBC) deposited onto Cu substrate for improving spallation behavior⁷, production of a Ni-Co/CoO FGM showing excellent electrochemical performance and subsequently corrosion behavior⁸, processing of laser assisted cladding with multi-graded layers aiming towards increased resistance to erosion and thermal stress induced cracking in molds for die casting⁹.

2. Multi-material components that are optimized for weight, size, or cost. Chin¹⁰ described how the defense industry can benefit from using FGMs in light and small components performing at the same or higher level than larger and heavier counterparts. Jutte et al.¹¹ demonstrated how FGMs can result in higher performance and reduced weight for the space exploration industry. Even though the main goal in such cases is to improve the component's performance with respect to a physical property, the developed components may be potentially exposed to corrosive environment during their lifetime. This can lead to severe corrosion attack as a result of galvanically coupled materials. In this respect, the corrosion performance of the FGMs deserve special attention. The material system in the present study is bi-metallic (substrate-overlaid block) with relevant compositional and distinct microstructural inhomogeneity. Thus, the above challenges for FGM are applicable to a large extent in the present material system.

Additive manufacturing (AM) is gaining widespread attention for its ability to produce high-quality structural metallic components with greatly reduced cost and improved lead-time^{12–14}. A wide variety of AM processes are currently available with different but also similar attributes¹⁵. In these processes, feedstock is melted or consolidated by an energy source in an incremental,

¹SINTEF Industry, Oslo, Norway. ²University of Ioannina, Department of Materials Science and Engineering, Ioannina, Greece. ✉email: amin.azar@sintef.no

layered manner through computer driven motion control. The outcome is a three-dimensional component created directly from a computer model without the use of molds or tooling open overlay panel¹⁶.

Despite the currently limited industrial adoption, there is a growing interest in AM of Al-alloys for building lightweight structures with complex geometries, high ratio of strength/stiffness to weight and good corrosion resistance¹⁷. Alongside technological progress, the process time and cost of AM of Al-based components can be greatly reduced^{15,18}. However, the production repeatability and reliability can be challenging due to factors such as presence of surface oxide scales, high thermal conductivity and large solidification shrinkage¹⁹.

Wire-arc additive manufacturing (WAAM) is a promising manufacturing technology of solid freeform fabrication owing to advantages, such as reduced time from concept to production, rapid processing, high density, materials saving, flexibility in materials and easy adaptability to automation²⁰. Owing to its high deposition rate, high material utilization rate, low production and equipment cost and high equipment flexibility and scalability, WAAM is more suitable for manufacturing large-scale components than other powder metallurgy AM techniques, where laser or electron beams are used as heat sources^{21–23}. However, the adoption of a conventional welding process for WAAM of aluminum is currently limited by solidification-due defects, like porosity and cracking²⁴. As-deposited WAAM-Al alloys have been found to possess inferior mechanical properties as compared to wrought counterparts and they have to undergo post-heat treatments²⁵.

The cold metal transfer (CMT) process is a modified version of gas metal arc welding (GMAW) based on a mechanism of controlled dip transfer^{26,27}. CMT yields high welding quality, low thermal heat input whilst it is nearly spatter-free²⁸. A combination of WAAM and CMT followed by an appropriate heat treatment may lead, through modification of the thermal profile, to a refined equiaxed microstructure and reduction of porosity²⁹. Owing to the aforementioned advantages, WAAM of Al-alloys combined with CMT is receiving an increasing interest from the aerospace industry. Recent studies^{30–32} have reported that a constant inter-pass temperature leads to an even distribution of material properties over the build-up geometry, whereas the mechanical properties depend on the direction of loading. Nevertheless, an Al-5Mg alloy manufactured by WAAM and polarity CMT exhibited a high tensile strength anisotropy between transverse and longitudinal tensile samples (8–27%), owing to the presence of interlayer micro pores³³.

So far, the vast majority of the corrosion studies on AM Al-alloys, refer to alloys prepared by SLM (mainly AlSi10Mg and to a much less extent Al12Si, Al-Cu (Al2024), AlSi50, Al-Zn (Al7075)). Sander et al.³⁴ and Kong et al.³⁵ have reviewed the recent studies extensively. Sander et al.³⁴ concluded that the effect of the AM microstructures on the corrosion of Al alloys is still not sufficiently understood. Kong et al.³⁵ identified the main factors affecting the corrosion degradation of SLM alloys: porosity, molten pool boundaries, surface roughness and microstructure anisotropy. Several corrosion studies comparing SLM and DMLS (direct metal laser sintering) Al-alloys with their wrought or cast counterparts have attributed the improved corrosion resistance of the SLM and DMLS alloys to their finer and more homogeneous microstructures^{36–39}. Cabrini et al.¹⁷ observed that the corrosion resistance of AlSi10Mg fabricated by DMLS in aerated dilute Harrison's solution was slightly reduced on planes perpendicular to the building plane. Similarly, Chen et al.⁴⁰ found that the x-z (parallel to the build direction) plane of SLM Al-12Si had better corrosion resistance in comparison with the x-y plane (parallel to the build plate) in 3.5 wt.% NaCl. In all AM technologies, the material is built on a substrate, which may have a significantly different chemical composition. This is mainly owing to the tendency to diversify the AM alloy compositions for technical reasons and the subsequent lack of an equivalent composition for the substrate

material. Post-deposition removal of the substrate from the deposited section and subsequent scraping can often be counter-productive. Therefore, in several applications, the substrate needs to remain as a part of the component to minimize the waste and cost. In these cases, a proper understanding of the corrosion performance of the system (substrate/deposited layers/fusion zones etc.) becomes important. Within the above framework and considering the scarcity of studies on the corrosion behavior of WAAM Al-alloys, the present effort investigates the corrosion performance of an AM aluminum alloy of the 5xxx series and its correlation with the microstructure of the deposited layers as well as the microstructure of the substrate.

The choice of 5xxx series is based on their distinguished combination of strength and corrosion resistance, as well as good weldability, that make them suitable for a broad range of industrial applications⁴¹. Although, 5xxx alloys cannot be hardened by aging (because Al does not form coherent precipitates with Mg), they exhibit the highest strength of all the non-age hardened series, through solution hardening (Mg has a high solubility in Al), dispersion hardening and strain hardening⁴². They are often used in applications in harsh environments, such as polluted atmosphere, industrial environments, and seawater. Typical examples are highway structures, bridges, storage tanks, pressure vessels, cryogenic systems for temperatures as low as -270°C and marine applications⁴³.

However, the Al-Mg alloys that contain Mg higher than 3.5 wt.% are susceptible to intergranular corrosion (IGC), stress corrosion cracking (SCC), and exfoliation corrosion (the latter in markedly directional structures) owing to the continuous intergranular precipitation of the highly anodic $\beta\text{-AlR}_6\text{RMgR}_5\text{R}$ or $\beta\text{-AlR}_3\text{RMgR}_2\text{R}$ phase^{44,45}. $\text{AlR}_6\text{R}(\text{Mn, Fe, Cr})$ particles, cathodic to Al⁴⁶, are also encountered in strain hardened and heat-treated Al 5xxx alloys^{47–49}. Moreover, MgR_2RSi particles, anodic to Al⁵⁰, are found in as-cast or wrought Al5xxx alloys^{44,47} and they are often associated with the $\text{AlR}_6\text{R}(\text{Mn, Fe})$ phase⁴⁴.

An issue that has to be addressed when dealing with the corrosion behavior of Al alloys (including the 5xxx and 6xxx series) is the effect of the Fe-containing intermetallic precipitates. Fe is the most common impurity in Al-alloys, even in commercially pure Al, forming with Al and Si a variety of brittle intermetallic compounds of acicular morphology⁵¹, identified as $\beta\text{-AlR}_5\text{RFeSi}$ ^{52–54} and/or $\delta\text{-AlR}_3\text{RFeSiR}_2$ ^{50,55}. The presence of other transition metals besides Fe, like Mn and Cr in trace amounts, can stabilize bcc phases, having a less-brittle Chinese-script morphology (e.g., $\alpha\text{-AlR}_{19}\text{RFeMnSiR}_2\text{R}$, $\alpha\text{-AlR}_{12}\text{R}(\text{FeMn})\text{R}_3\text{RSi}$, $\alpha\text{-AlR}_{12}\text{R}(\text{Fe, Cr})\text{R}_3\text{RSi}$ ^{55,56} or a compact blocky morphology ($\alpha\text{-AlR}_{15}\text{R}(\text{Fe, Mn})\text{R}_3\text{RSiR}_2\text{R}$ ⁵⁷. $\alpha\text{-Al}(\text{Mn, Fe})\text{Si}$ ($\text{AlR}_8\text{RFeMnSiR}_2\text{R}$ or $\text{AlR}_{12}\text{R}(\text{Fe, Mn})\text{R}_3\text{RSi}$) are microstructural features in as-cast, homogenized and strain hardened Al 5xxx alloys^{47,58,59}. The cathodic role of the Al-Fe-based intermetallic impurities in the corrosion of Al-alloys and composites is well-established^{46,50,60,61}. Al-Fe based intermetallic compounds are nobler than Al, particularly when Al is alloyed with the extremely anodic Mg⁴⁶.

RESULTS AND DISCUSSION

Deposition and characterization of the as-received material

Figure 1a, b illustrate the computer aided design (CAD) representation of the block geometry compared to the deposited material. The dimensions of the deposited block are $\sim 20 \times 10 \times 5$ cm. The inter-pass temperature was controlled to reach below 120°C before a new bead was deposited. The obtained stress-strain curves are shown in Fig. 1c, d. Note that the tensile tests were carried out only for the deposited material and the results do not reflect the strength of the interface between the two alloys. The tensile test specimens were in as-deposited and homogenized conditions. Round tensile samples were extracted along x, y, and z directions, complying with the ASTM E8M-04, with the parallel section diameter of 6 mm, and gauge length of

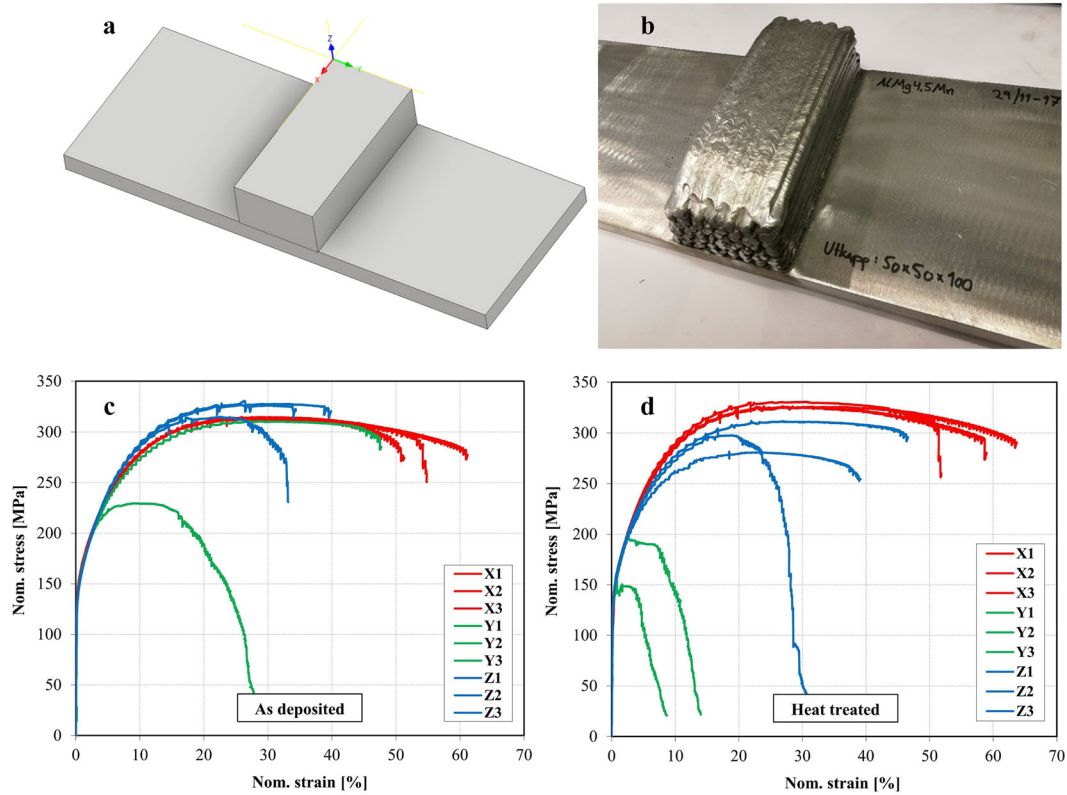


Fig. 1 The deposited material and the corresponding stress–strain curves of the deposited alloy in x -, y -, and z -directions. **a** Nominal CAD geometry; **b** Actual deposited geometry; **c** Tensile results of the as-deposited materials; **d** Tensile results in heat-treated (homogenized) condition.

30 mm. Homogenization heat treatment was performed at 400 °C for 4 h, only towards identifying the effect of chemical composition inhomogeneity on the mechanical behavior.

The tensile strength and elongation at break along the x (deposition) direction show consistent and acceptable mechanical performance. Although the homogenized material shows somewhat higher ultimate tensile strength compared to the as-deposited material along the deposition path, the overall behavior is quite identical before and after heat treatment. In the as-deposited condition, the tensile curves along the y and z directions—where the interfaces between each deposited bead come into play—show degraded properties. The original hypothesis was whether chemical inhomogeneity, especially on the fusion line and interfaces between adjacent deposited beads, could be the root cause. However, the same type of behavior was also observed after the homogenization heat treatment. This observation suggests that there is another mechanism that governs the mechanical response of the material along different orientations. Later in this section, it will be explained that the abundance and special positioning of the precipitates on the fusion lines of the deposited beads is a possible explanation for the inferior mechanical and corrosion performance of the deposited material.

Figure 2a–d presents SEM micrographs from different zones of the as-received material (x - y plane). All zones exhibit uniform dispersions of particles that were identified by energy-dispersive spectroscopy (EDS) as mostly being Al-Fe-Mn-Si (or Al(Fe, Mn)Si) intermetallic compounds, in compatibility with^{47,55–59}. Some Al-Fe-Mn (or Al(Fe, Mn)) particles have also been identified in the deposited alloy, in compliance with findings of other researchers^{44,47–49}.

The Al6061-T6 substrate contains coarse second phase particles directionally distributed in the matrix. The coarse particles appear to a great extent polygonal and more rounded as compared to original needle-like AlFeSi particles, due to the solution treatment,

as well as the presence of Mn⁶². The directional precipitation in Al6061-T6 has previously been associated with the precipitation of insoluble Al(Fe, Cr)Si and excess soluble Mg₂Si particles along the grain boundaries (elongated due to work hardening)⁶². In the present case, Mg₂Si particles could not be discerned, neither by SEM nor by EDX, because: (a) the Mg₂Si phase has largely been dissolved in the Al-matrix due to the solution treatment, and (b) the semi-coherent β' -Mg₂Si precipitates in the matrix (due to aging) are ultra-fine (besides, β' -Mg₂Si precipitates need a special etching technique to be discerned, which is out of the scope of the present paper). The substrate/deposited alloy interface is characterized by finer precipitates than those of the substrate but still coarser than those in the deposited material.

The interlayer boundaries and the overlayer interior are characterized by a similar microstructure in terms of precipitation extent, particle size, shape, and distribution. Fine particle size and spheroidal or short rod-like shape of the dispersed phase of the deposited block can be ascribed to the higher amount of Mn and Cr and the lower amount of Si in the 5083 alloy, as shown previously, Mn and Cr accelerate the transformation of acicular β -AlFeSi to the more equiaxed α -AlFeSi phase, whereas Si decelerates it⁶³. Therefore, the aforementioned differences in the microstructures of the substrate alloy, substrate/deposited alloy fusion zone and the deposited alloy can pose a threat on the overall performance of the AM structure.

Homogenization heat treatment was applied on the deposited materials. It was observed that the partitioned Mg content in the as-deposited condition dissolves into the matrix after homogenization. Therefore, the homogeneity of the improved microstructure does not explain the observed loss in the structural integrity and its mechanical behavior. The degraded mechanical properties echo a heat treatment induced phenomenon that will be scrutinized later in this section.

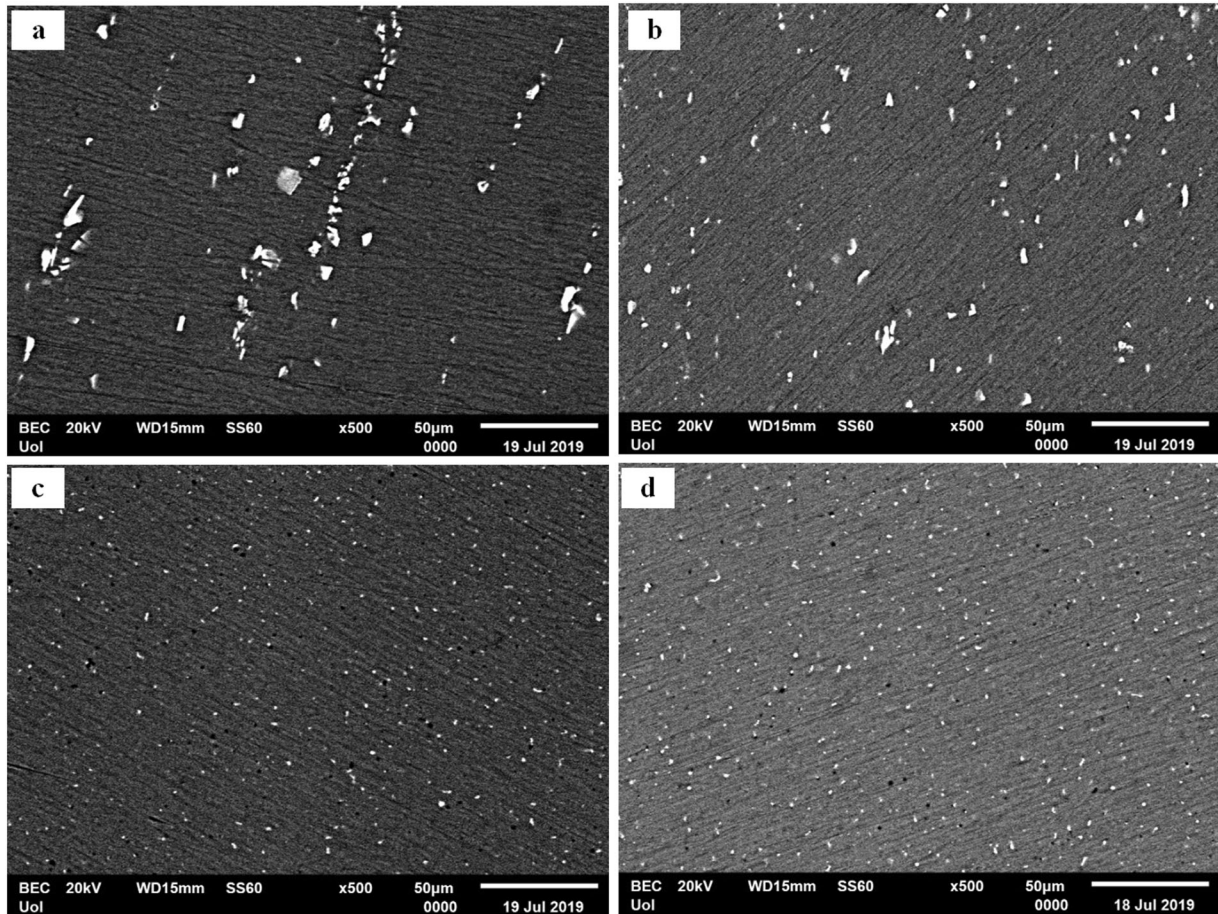


Fig. 2 SEM micrographs (BEC mode) of the as-received structure (x-y plane). a zone a: substrate; b zone b: substrate/deposited alloy interface; c zone c: interlayer boundaries; d zone d: within a deposition layer.

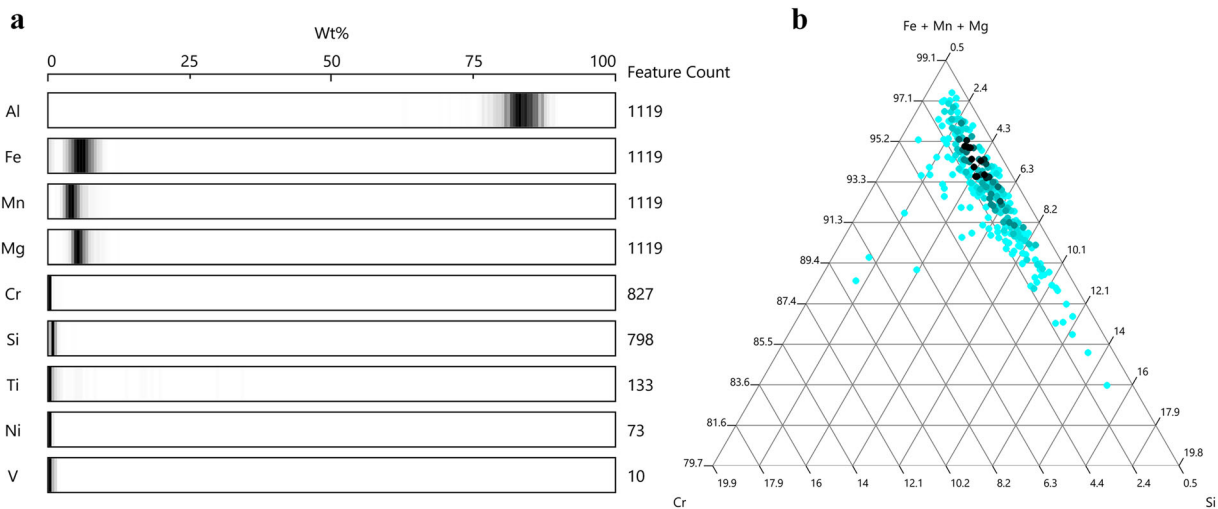


Fig. 3 Abundance and distribution of elements in the analyzed particles. a Weight normalized genome graph; **b** Ternary phase diagram showing the content of Cr and Si elements as second and third most abundant elements in the particles of this alloy.

Further exploration of the microstructure shows the presence of needle shape precipitates, mostly in the interlayer regions (fusion lines).

In this study, a length of 6.5 mm that crosses over three deposition layers was investigated. The number of analyzed

particles in the inspected area was 1119 counts. Figure 3 depicts the results of particle chemistry analysis. The Genome graph in Fig. 3a shows that all of the 1119 analyzed particles were found rich in Fe, Mn, and Mg, while 74%, 71%, 12%, 6.5%, and 0.9% of the particles contained Cr, Si, Ti, Ni and V, respectively. Figure 3b

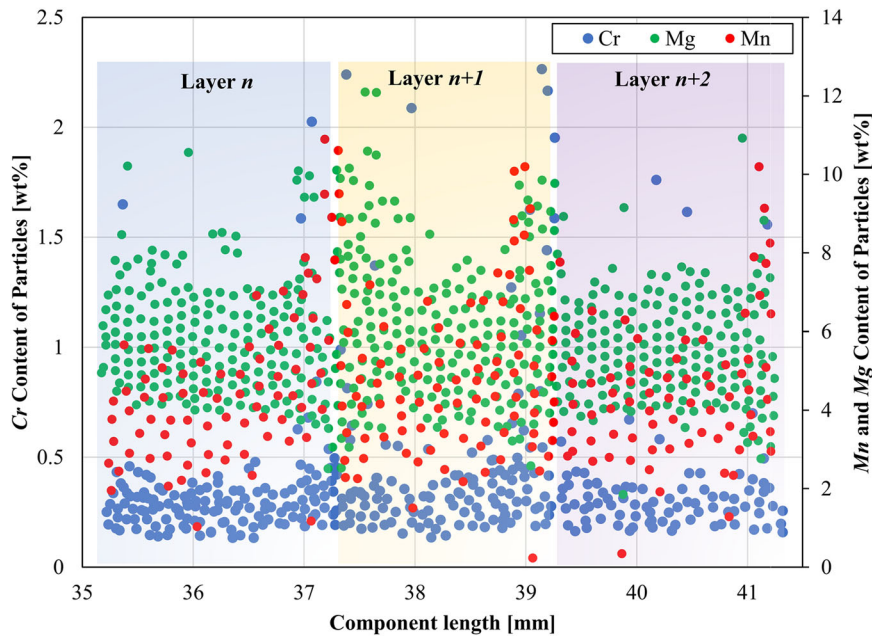


Fig. 4 Distribution of the elements along the build direction. The illustration shows that the particles contain larger amounts of Cr, Mn, and Mg on the fusion lines.

illustrates the distribution of the particles on a ternary phase diagram. In this illustration, the distribution of the three dominating elements in the particles, namely Fe, Mn, and Mg are mapped against the second and the third most abundant elements in the particles (Cr and Si). According to this illustration, the analyzed particles in addition to Fe, Mn, and Mg contained Si in a relatively wide compositional range, while the same particles hardly showed Cr at contents above 2 wt%.

Another important finding is the location dependency of the content of certain elements in the investigated particles. Figure 4 maps the weight percentages of Cr, Mn, and Mg in analyzed particles across three deposition layers of AA5083. Inside the deposited material, the contents of these elements are scattering within a few wt.% range. However, at the interlayer boundaries (fusion lines) the analyzed particles seem to be richer in Cr, Mn, and Mg. In other words, the thermal gradient during multiple layer deposition gives rise to localized presence of particles along the fusion boundaries with different composition. The evolution of particles with higher Cr, Mn, and Mg content suggests that the alloying elements in the matrix can also be influenced. Whether this phenomenon affects the corrosion performance, will be investigated later in this section. Evolution of these particles may also explain the anisotropic mechanical performance of the material shown in Fig. 1c, d.

The microstructures of the intermetallic dispersed phases reveal that during deposition and subsequent cooling, dissolution and recrystallization processes have taken place. At the interlayer boundaries of the as-received AM alloy, needle-like Fe-rich particles were occasionally observed (Fig. 5). These precipitates are rich in Al, Fe, Mn, and Si and correspond to Al(Fe, Mn)Si intermetallic particles that were not partially dissolved during deposition to finally produce fine Al(Fe, Mn)Si particles. Figure 5 also reveals fine dispersoids that are rich in Fe, Mn, Si, and/or Ti. The samples were electropolished to reveal the needle shape particles without which, they could not be vividly presented.

Corrosion performance of the as-received AM material

The cyclic potentiodynamic polarization curves of the different zones of the AM sample (surfaces parallel to the y-z plane) during

immersion in 3.5 wt.% NaCl at 25 °C are shown in Fig. 6a. It can be seen that despite the microstructural differences of the four zones, the polarization performances with respect to the corrosion potential (E_{corr}), pitting potential (E_{pit}), forward and reverse curve shapes, onset potential of current stabilization and current stabilization values are similar. The mean corrosion potential values for the tested surfaces of “substrate/coating interface”, “within an overlayer”, and “interlayer boundaries” are -709 ± 15 , -744 ± 20 , and -705 ± 1 mV vs. Ag/AgCl, respectively; the mean pitting potential values for the tested surfaces of “substrate/coating interface”, “within an overlayer”, and “interlayer boundaries” are -685 ± 24 , -695 ± 21 , -687 ± 26 mV vs. Ag/AgCl, respectively. All zones have suffered from localized corrosion, as suggested by the flat gradient of the anodic polarization curves, which is sustained for current densities of more than three orders of magnitude. The negative hysteresis loops of the cyclic polarization curves and their large surface areas enhance the above indications for occurrence of localized corrosion. The shapes of the anodic polarization portions are characteristic for aluminum and its alloys in aerated aqueous NaCl^{64–66}. Pitting potentials are almost equal (in one out of three of the anodic curves of the “substrate/coating interface” and “interlayer boundaries” zones) or just a few tens of mV higher than the corrosion potential, suggesting that aluminum is readily polarized to its pitting potential⁶⁷; in other words, localized corrosion has already taken place during the open-circuit state⁴² and/or during cathodic polarization⁶⁸. Hence, it is inferred that the corrosion of the aluminum matrix in all zones controls the overall corrosion mechanism.

The only distinct difference in the polarization performance of the four zones lies in the cathodic polarization curves. It is seen that cathodic current values follow the sequence: substrate > substrate/coating interface > interlayer boundaries > within an individual deposited layer. This sequence indicates that the Al6061 substrate owns the largest cathodic particle surface area, and the interior of each deposition layer owns the smallest cathodic particle surface area.

Figure 6b compares the potentiodynamic polarization curves (forward scans) of surfaces parallel to the y-z and x-z planes. These planes and substrate do not present significant differences with

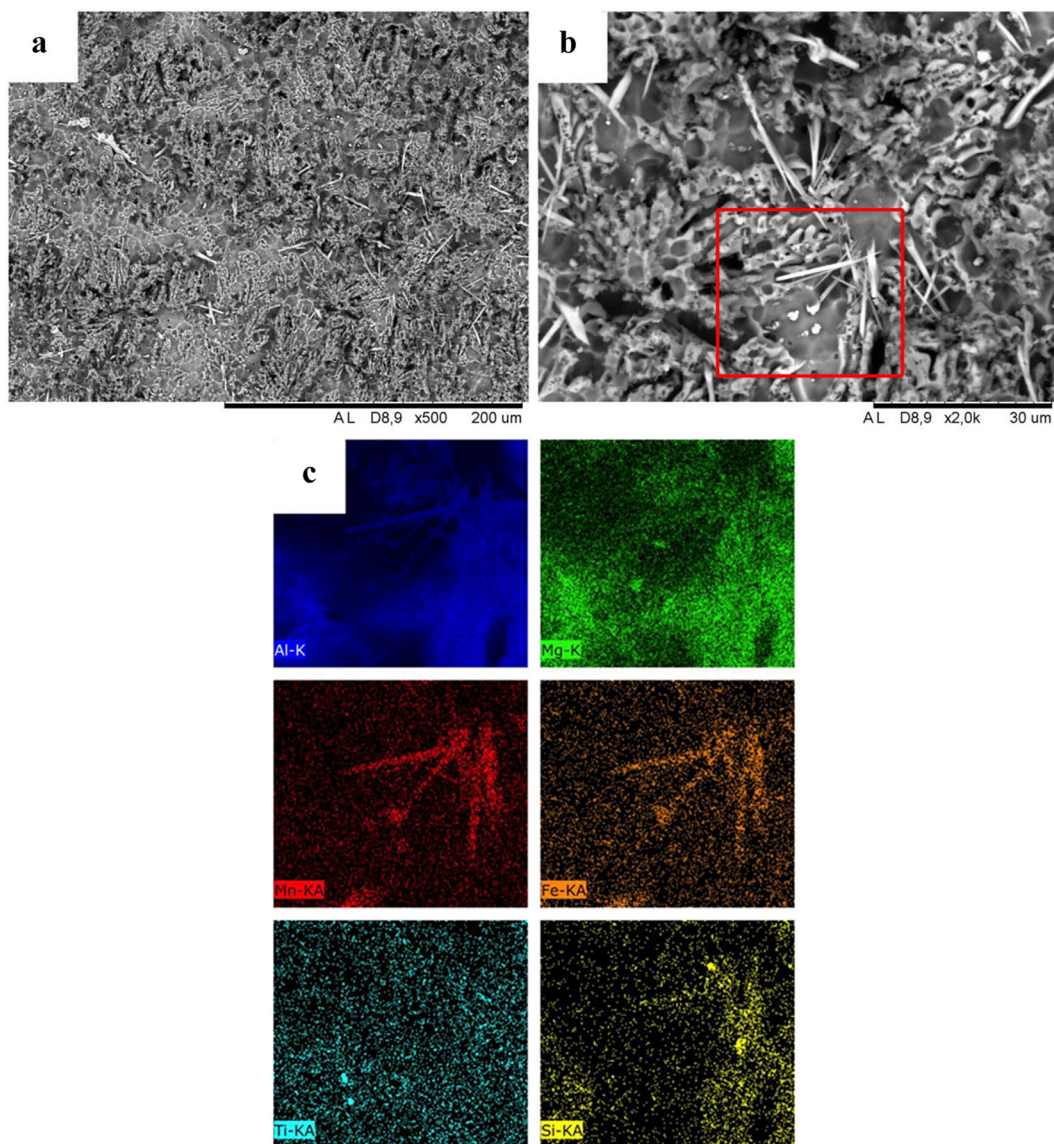


Fig. 5 Images of accumulated intermetallic particles between the deposited beads. **a** shows the interface in which many such particles can be seen; **b** shows a magnified image of the needle-shaped particles; **c** shows the elemental maps of Al (blue), Mg (green), Mn (red), Fe (orange), Ti (cyan), and Si (yellow).

respect to the anodic polarization behavior. Differences are rather greater in the case of the cathodic polarization curves. Furthermore, the same sequence (as in the y - z plane) in the cathodic current values of the four zones is followed.

Figure 6c compares the potentiodynamic polarization curves (forward scans) of overlayers located at different distances from the substrate (parallel to the y - z and x - z planes). The polarization curves of the Z2 and Z4 surfaces, parallel to the x - z plane (their centers were located at 2.0 and 5.5 cm (respectively) away from the substrate/deposited alloy boundary) are similar with the exception of small differences between the cathodic current densities. More distinct differences are observed in the (anodic and cathodic) polarization curves of the Z2 and Z3 surfaces parallel to the y - z plane, the centers of which were located at 2.0 and 4.0 cm (respectively) away from the substrate/deposited alloy boundary. Therefore, it is indicated that the deposited AM alloy parallel to the x - z plane is somewhat more isotropic through its thickness than the deposited AM alloy parallel to the y - z plane.

Figure 7 shows that the corrosion of the 6061 substrate presents a strongly localized character with deep crevices.

Corrosion at the substrate-deposition interface has progressed to a shallower depth than that of the substrate, but intergranular corrosion is more extensive (Fig. 7b). The intensively wavy (excavated-like) surfaces of the interlayer boundaries and the deposited layers in Fig. 7c, d, respectively, reveal higher surface material removal for the deposited block as compared to the substrate and the primary fusion zone. However, the localized manifestations in the deposited alloy have proceeded to a much lower depth than that of its substrate and substrate/deposited alloy interface.

The governing form of the substrate (zone a) corrosion appears to be pitting of Al around second phase particles that has evolved to crevice corrosion that are of Al(Fe, Mn)Si intermetallic type.

The degradation features of the substrate/deposition interface (zone b) show abundant signs of IGC, unbranched cracking and material detachment (mostly intergranular). Large zones appear totally oxidized. IGC of Al is associated with increased intergranular concentration of Si and Fe and intergranular Al(Fe, Mn)Si intermetallic phases. The possibility of stress corrosion cracking is indicated by the presence of intergranular cracks. The extensive

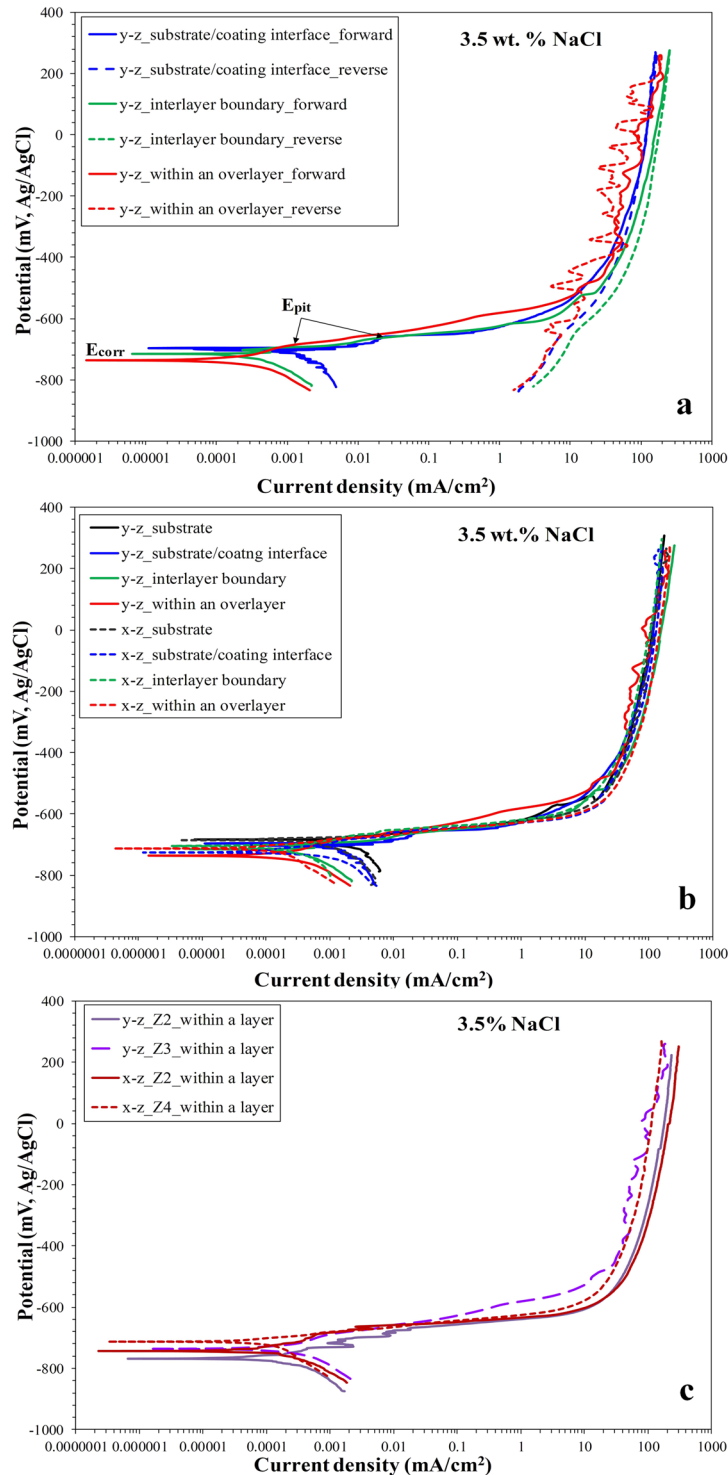


Fig. 6 Polarization curves. **a** Cyclic polarization curves of the different zones of the AM structure (surfaces parallel to the y-z plane); **b** Comparison of forward polarization curves of surfaces parallel to the y-z and x-z planes; **c** Comparison of forward polarization curves of surfaces parallel to the y-z and x-z planes at distances Z2: ~2.0 cm, Z3: ~4.0 cm and Z4: ~5.5 cm from the substrate (3.5 wt.% NaCl, 25 °C).

intergranular degradation hints the presence of intergranular submicron/nano-precipitates.

Figure 8a, b reveal pitting around fine and submicron particles at the interlayer boundaries (zone c) and within the individual overlayers (zone d), respectively. EDS analysis reveals that the large majority of the intermetallic particles are of the type Al-Fe-Mn-Si, Al-Fe-Mn, Al-Fe-Mn-Cr-Si (Fig. 8a, sp. +, Fig. 8b, sp. •). Al-Fe-Mn-Ti-Cr-Si and Al-Ti-Fe-Mn intermetallics have also been

detected by EDS. Therefore, the surface material removal in Fig. 7c, d can be attributed to the intergranular dissolution of the (Al, Mg) matrix and the subsequent dislodgement of the dispersed fine particles. IGC is associated with the increased IG presence of Fe (Fig. 8b, sp. *).

The observations in this section manifest that the Al(Fe, Mn)Si-based intermetallic particles play the most important role in the corrosion behavior of the system. The coarseness of the Al(Fe, Mn)

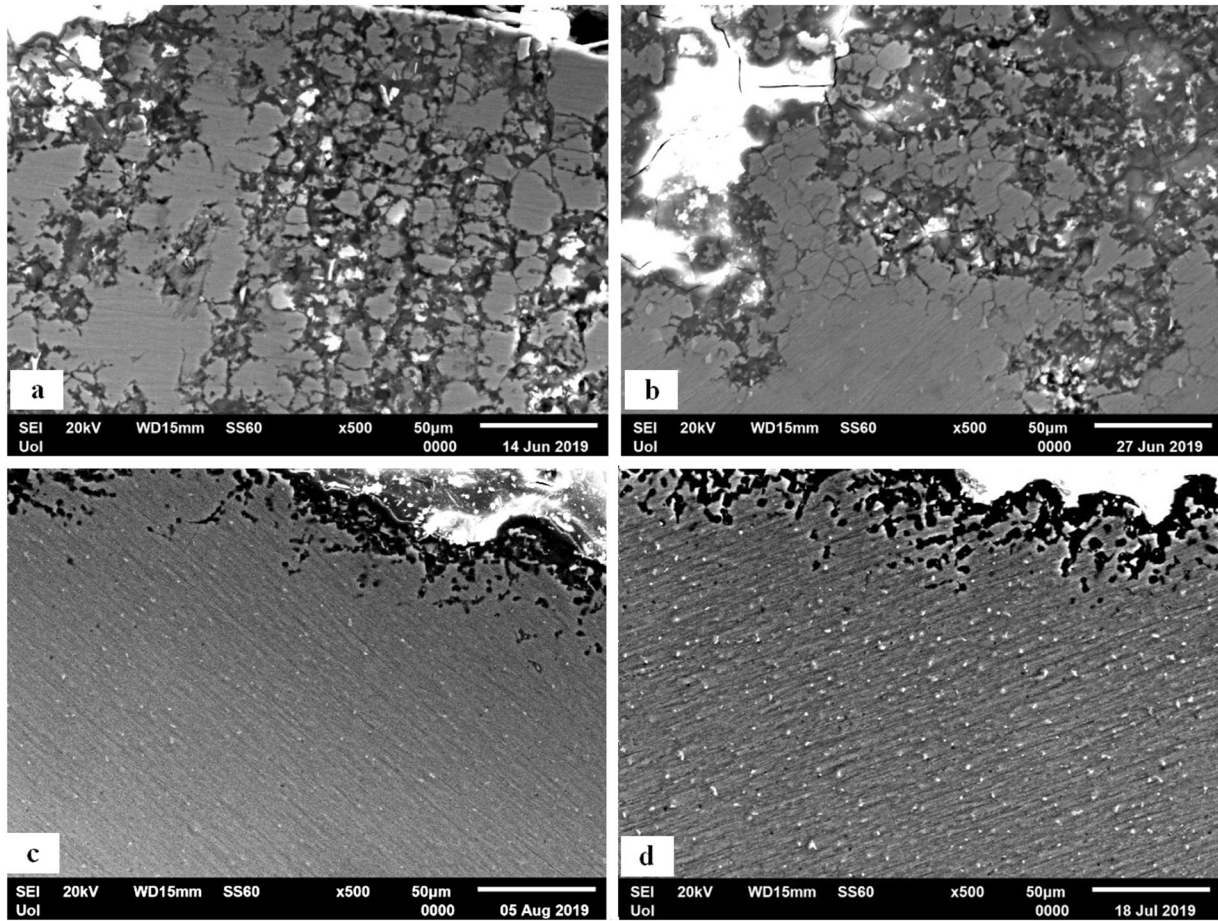


Fig. 7 Overview SEM micrographs of the corroded cross-sections. a Substrate; **b** Substrate-deposition interface, **c** Interlayer boundaries, and **d** Within a deposition layer.

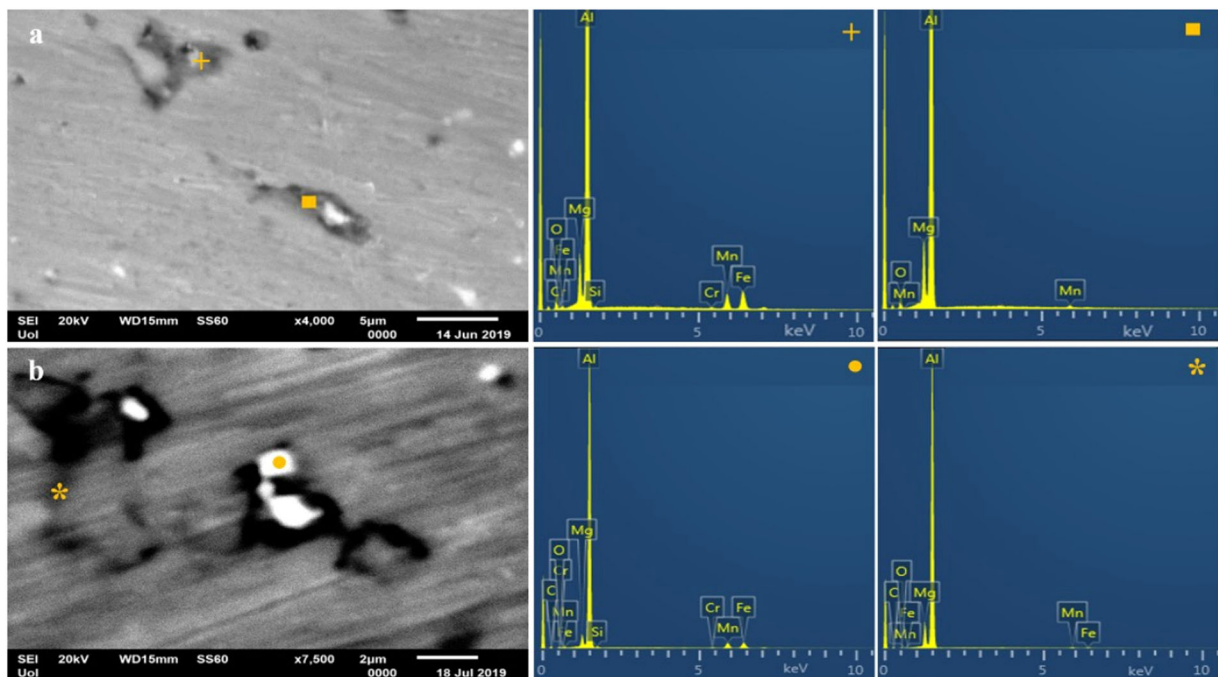


Fig. 8 Cross-sectional micrographs after corrosion testing. a Interlayer boundaries (zone c) showing preferential corrosion of the Al-Mg matrix (sp. ■) around Al-Fe-Mn-Cr-Si (sp.+) particles; **b** Within an overlayer (zone d) showing preferential corrosion of the Al-Mg matrix around Al-Fe-Mn-Si-Cr precipitates (sp. •) and IGC associated with the intergranular presence of Fe (sp.*).

Si-based intermetallic particles along with their directionality are the main reasons for the intensively localized corrosion behavior of the substrate and the substrate/deposited alloy interface as compared to that of the overlayers. The coarse cathodic surfaces can obviously support cathodic reactions more efficiently than the fine ones. Moreover, the directionality of the Al(Fe, Mn)Si particles in the substrate as well as the intergranular degradation in both the substrate and the substrate/deposited alloy interface show that the Al(Fe, Mn)Si phase forms a network predominantly interconnected (Fig. 7a, b). As the anode is gradually consumed with corrosion progressing, the already high total cathodic surface area-to-total anodic surface area ratio further increases because of the large surface area of the Al(Fe, Mn)Si network^{61,69}. This phenomenon results in a rapid and intensive corrosion effect.

The cathodic Al(Fe, Mn)Si intermetallic particles in the deposited layers (interior and interlayer boundaries) is also responsible for the degradation. The particles are form a homogeneously and relatively dense distribution, probably as an interconnected network (see Fig. 8b). Although the individual precipitates are comparatively fine to provide as an effective support to cathodic reactions as the coarse ones (in the case of the substrate and substrate/coating interface), their dense dispersion provides a fine network of cathodic boundaries that results in a significant total cathodic surface area-to-total anodic surface area ratio. Moreover, the inclusion of elements like Cr and Ti further increases the nobility of the cathodic precipitates (as Cr and Ti can stabilize the weak passive film formed on the Al-Fe-based intermetallics⁴⁶), enhancing the galvanic effect between the Al(Fe, Mn)Si particles and the adjacent matrix. Consequently, degradation along this fine network takes place, leading to surface material removal that is more extensive in comparison with that of the substrate. However, it proceeds to a shallower depth compared to the corrosion of the substrate and the substrate/primary layer interface.

To summarize, the microstructural observations of the corroded cross-sections are compatible with the polarization results in the following manner:

1. The susceptibility to localized corrosion, suggested by the negative hysteresis loops of the cyclic polarization curves as well as the sharp and sustainable anodic current increase at potentials very close to the pitting potential of Al, has been confirmed by the main corrosion forms identified in all zones of the AM system (substrate: pitting and crevice, substrate/deposited alloy interface: pitting, intergranular corrosion and stress corrosion cracking, deposited layers (boundaries and interior): pitting and intergranular).
2. The highest cathodic current values recorded for the substrate can be explained by the presence of the coarsest Al(Fe, Mn)Si intermetallic compounds (Fig. 7) that provide the largest cathodic surfaces to support cathodic reaction and, consequently, the greatest galvanic effect between the intermetallic particles and the aluminum matrix.
3. The substrate/deposited alloy interface yields cathodic current values that are lower than those of the substrate, but higher than those of the deposited layers in compatibility with the intermetallic Al(Fe, Mn)Si particles. Such particles are finer than those of the substrate, yet coarser than those in the deposited layers (Fig. 7).
4. The similar polarization behavior of the boundaries and interior of each individual deposited layer can be attributed to the similar microstructure in terms of dispersed particle extent, particle size, shape, and distribution (Fig. 7).

Topography mapping results on the AM sample after the corrosion test are shown in Fig. 9. The surface of the deposited material appears rougher than that of the substrate (height step present at the substrate/deposition interface), in agreement with the wavy, excavated-like surfaces of the overview cross-sectional

micrographs of Fig. 7c, d. The interlayer boundaries (zone c) appear deeper than the surrounding bead material, making the individual layers (zone d) distinct both on the overview and the detail topography maps. Hence, the respective postulation put forward in the results section for a higher surface material from the interlayer boundaries as compared to the layer interior is herein confirmed. While the substrate appears to have lost less surface material than the deposited layers, deep corrosion pits are apparent in both the substrate (zone a) and the substrate/deposited layer interface (zone b). Pits appear dispersed on the surface of the substrate in agreement with Fig. 7a. Conical pits wide and shallow at the surface but narrow and deep at the bottom are observed at the substrate/interface vicinity. These wide (at the surface) pits are localized within the primary deposition-due heat affected zone suggesting that the thermal history of the alloy, affecting its corrosion properties. The extensive IGC along with intergranular stress corrosion cracks of zone b (Fig. 7b) enhance the above consideration. The topography measurements thus corroborate the microstructural observations.

X-ray photoelectron spectroscopy (XPS) analysis in Fig. 10 shows that the corroded surface of the deposited material is mainly composed of aluminum oxide with the presence of carbon and fluorine contaminations, as well as small amounts of magnesium, sodium and chlorine, in compatibility with previous XPS studies on the corrosion products of 5xxx alloys^{70–72}. Silicon is barely observed, while neither iron nor manganese are detected, in agreement with^{70–72}. Regarding Si and Fe, their concentrations in the deposited alloy are only 0.1 wt.% and 0.2 wt.%, respectively, and they become even lower in the outer surface oxides/hydroxides and chlorine complexes. As such, their presence in the outermost surface can be masked by the abundant presence of Al and Mg. Regarding Mn (0.8 wt.% in the deposited alloy), its participation in the outer part of the passive film of Al-Mn alloys (Mn \geq 1 wt.%) in chloride media has also been found negligible in previous works^{73–75}. According to Zhang et al.⁷⁴, Mn may be present in the surface film only as an impurity and does not influence the electronic structure of the film.

Detailed spectra of Al and Mg peaks do not show multiple chemical states (Fig. 10b, c). The peak positions fit well with oxidized species of these elements, the precise chemical state cannot be determined with certainty. The XPS maps for Al and O in Fig. 10d show that the corroded surface has been uniformly covered by an Al-oxide/hydroxide-based film.

The presence of Na peaks is attributed to residual electrolyte, despite a thorough rinsing of the surfaces under deionized water before XPS scanning. However, the presence of Cl peaks can only partly be attributed to the residual electrolyte. The intensive presence of Cl in surface parts denuded of Na, as shown in the XPS map of Fig. 10d, indicates that Cl peaks are partly owing to chlorine adsorption in the outer layer of the surface film; the adsorption of chlorine in the outer layer of the surface film of Al-alloys has been well-documented^{74,76–78}. Therefore, the XPS results suggest that one reason for the high current values in the current stabilization stage is the deposition of unstable products (heavily hydrated structures, like hydrated oxides and chlorine complexes) in the pits/crevices.

In all zones of the layered material system, corrosion has mainly been induced by the large electrochemical potential difference between (Al, Mg) and Al(Fe, Mn)Si intermetallic compounds. This electrochemical potential difference becomes even bigger considering the following established statements: (a) Locally (i.e., around cathodic intermetallic inclusions) alkaline pHs result from the cathodic reaction of oxygen reduction $O_2 + 2H_2O + 4e^- \rightarrow 4OH^-$ on the intermetallic precipitate sites⁷⁷. The cathodic dissolution of Al can also cause a significant local pH increase⁷⁹. (b) The passive film of the Al-Fe-based intermetallic compounds at alkaline pHs is thermodynamically stable⁸⁰. (c) Al_2O_3 is soluble at alkaline pHs⁸¹. Therefore, in the present effort, dissolution of the

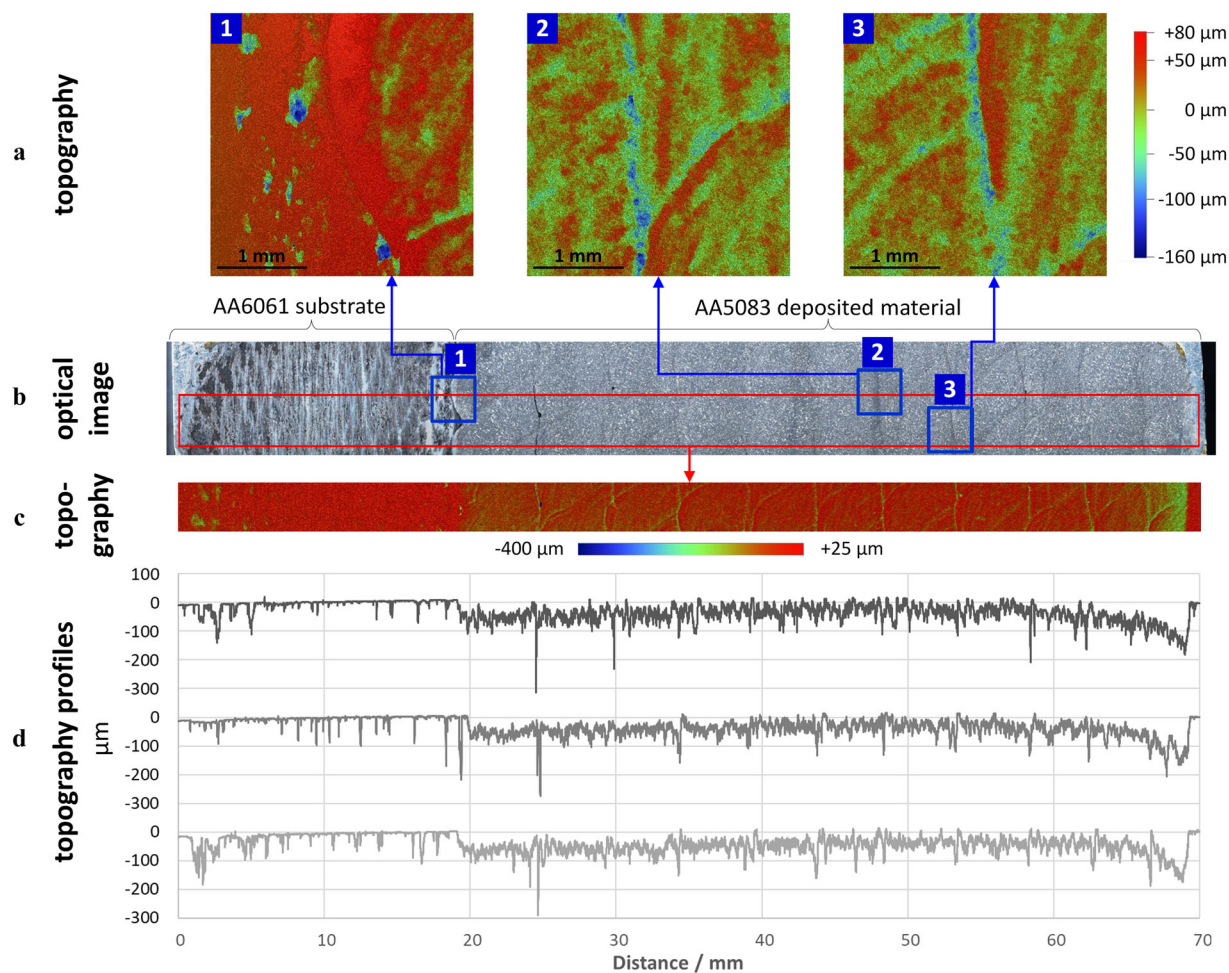


Fig. 9 Topography mapping results of the corroded sample. **a** High-resolution map of the transition between substrate and deposited layers (left) and of two-layer interfaces; **b, c** Optical image with the positions of the topography measurements and topography mapping over the whole length of the sample; **d** Three topography profiles extracted from the large area mapping.

alumina film on the surface of the Al-matrix adjacent to the Al-Fe-Si-Mn precipitates has occurred, which has been accentuated by the cathodic polarization that preceded anodic polarization. The Al(Fe, Mn)Si particle size, preferential location/orientation and inclusion of noble elements (Cr, Ti) also play important roles on the governing corrosion form and progress, as discussed in previously in this section.

Based on the electrochemical and microstructure observations, as well as the aforementioned statements, corrosion degradation is postulated to have proceeded via the following steps:

- (i) chloride adsorption on the alumina surface film, selectively at the interfaces between incoherent precipitates, like Al(Fe, Mn)Si and the (Al, Mg) matrix. (The presence of Cl in the outer surface layer was detected by XPS (see Fig. 10).
- (ii) chemical reaction of the adsorbed chloride with the aluminum anion in the aluminum oxide/hydroxide lattice, as reported in⁷⁶.
- (iii) accelerated surface film thinning at the interface by dissolution⁷⁶. As aforementioned, the alumina film is soluble in the locally alkaline pHs generated from the oxygen reduction reaction and dissolves in its flaws.
- (iv) direct and concentrated galvanic attack on the matrix under the thinned film amplified by the electrochemical potential difference between the matrix and Al(Fe, Mn)Si-based intermetallic compounds and formation of small pits.
- (v) deepening of the pit, as pitting is an autocatalytic process⁸²,

and formation of differential aeration cells between the pit bottom and the pit walls.

- (vi) acidification of the growing pits due to aluminum hydrolysis reactions: $\text{Al}^{3+} + 3\text{H}_2\text{O} \rightarrow \text{Al}(\text{OH})_3 + 3\text{H}^+$; The local pit environment becomes depleted in oxygen (i.e., the cathodic reactant), whilst enriched in Al^{3+} and Cl^- . The latter electro-migrates into the pit to maintain charge neutrality.
- (vii) pit propagation under the acidic chloride environment in the pits.
- (viii) in the case of the substrate and the substrate/deposited alloy interface, pit merging and evolution to crevice corrosion (substrate) or IGC (substrate/coating interface).
- (ix) in the case of the deposited layers, pit merging and evolution to IGC. (The fine and relatively dense dispersion of Al(Fe, Mn)Si particles, often including galvanic effect enhancers, such as Cr and Ti, promotes IGC and a relatively extensive surface material removal.) The dislodgement of fine intermetallic particles causes a reduction of the cathodic surface area-to-the anodic surface area ratio that eventually hampers IGC. Corrosion further proceeds through localized degradation of Al adjacent to the Al(Fe, Mn)Si particles.

The delineated mechanism was shown to occur in previous works, where Fe impurities in the form of Al-Fe-Si intermetallic compounds are present in the Al-alloys in minor amounts or traces^{50,83}.

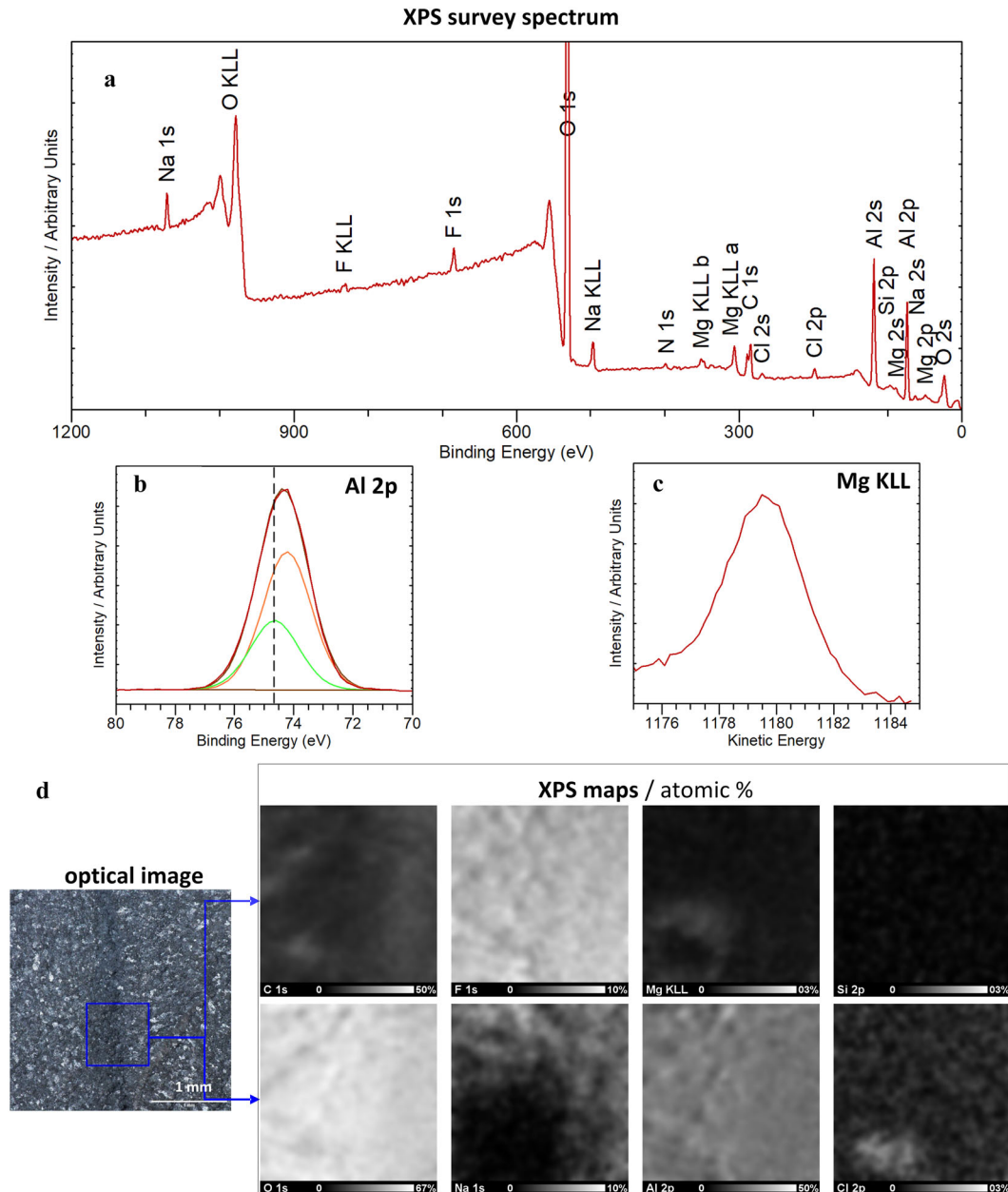


Fig. 10 XPS results from the corrode surface of the deposited layer. **a** XPS survey spectrum from a region covering parts of two beads; **b** Al 2p fitted with a single spin-orbit pair; **c** Mg KLL detail spectra, and **d** Optical image with the XPS mapping area marked (left) and quantitative XPS maps of the detected elements.

Based on the discussions above, the following can be deduced:

- WAAM combined with CMT process is able to deposit a multi-layered Al5083-type alloy on an Al-6061 substrate.
- The substrate, substrate/deposited alloy interface, interlayer boundaries and deposited layers interior presented a microstructure mostly consisting of Al(Fe, Mn)Si intermetallic particles uniformly dispersed within an Al-Mg matrix. The coarseness of the dispersed particles followed the sequence: substrate > substrate/deposited alloy interface > interlayer boundaries ≈ deposited layer interior. The fine particle size of the dispersed phase in the deposited block is attributed to higher Mn, Cr and lower Si contents as compared to the substrate.
- The observed particles in the fusion line region affect the mechanical properties of the material along the transverse directions, namely y - and z - direction.
- The interlayer boundaries presented an increased concentration of Cr, Mn, and Mg relative to the interior of the deposited layers.
- The main corrosion forms identified in the various zones of the AM system are substrate: pitting and crevice corrosion, substrate/deposited alloy interface: pitting, intergranular corrosion, and stress corrosion cracking, overlayers (boundaries and interior): pitting and intergranular corrosion.
- After the deposition process, heat treatment of the material has been performed. Despite the fact that the microstructure becomes more homogenous, the corrosion tests results on the as-deposited condition do not suggest any significant impact on the corrosion performance since the main influential microstructural features were identified as interlayer precipitates.
- The corrosion degradation of the Al6061-T6 substrate was mainly due to the presence of coarse Al(Fe, Mn)Si particles and

their directional alignment. The corrosion degradation of the Al6061-T6 substrate/Al5083 deposited block interface was mainly due to the presence of coarse Al(Fe, Mn)Si particles forming a continuous intergranular network with Fe-rich submicron precipitates and the exertion of residual stresses.

- The corrosion degradation of Al-5083 AM-deposited on Al6061-T6 was mainly due to the presence of AlFeSi (usually containing Mn, often Cr, occasionally Ti) precipitates that are highly cathodic (especially the ones containing Cr and/or Ti) to the Al-matrix.
- The interior of the deposited layers and the interlayer boundaries exhibited similar polarization behavior (along x - z and y - z planes), as well as similar microstructure and surface chemistry after corrosion testing. The y - z and x - z planes of the deposited block did not present significant differences in terms of anodic polarization behavior. Differences were more distinct in the case of the cathodic polarization curves. The deposited block parallel to the x - z plane presented a somewhat higher isotropy in the electrochemical performance through its thickness than the deposited AM alloy parallel to the y - z plane.
- Both the substrate and the substrate/deposited block interface manifested an intensively localized behavior with deep crevices (substrate) and deep intergranular cracks/pits. On the other hand, the deposited layers and their boundaries presented a greater removal of surface material (uniform as a result of intergranular corrosion) but shallower pits and absence of IG cracks.
- A more suitable substrate (possibly of the 5xxx group that finds wide application in marine environments) could be tested towards an improvement of the galvanic compatibility between substrate and deposited alloy. This suggestion is also supported by the fact that the microstructure of the substrate/deposited alloy interface was governed by the microstructure of the substrate. Besides, the substrate/deposited alloy interface was the only zone that exhibited stress corrosion cracking, suggesting the existence of residual stresses.

Future work

Based on the advanced characterization results, mechanical response, and overall observations of the material performance, it can be confidently claimed that the inhomogeneous and uneven distribution of the precipitates is the governing phenomenon that explains the anisotropic properties and local corrosion attacks. Precipitation mechanisms in aluminum alloys is a complex and challenging aspect. One viable approach is to define the AM processing window away from the precipitation range. In most of the precipitation strengthened aluminum alloys, the temperature range for evolution of precipitates is usually below 400 °C⁸⁴. One plausible hypothesis would be to hold the inter-pass temperature above this threshold to avoid formation of the precipitates between each two adjacent layers. Since the thermal conductivity of aluminum is relatively high, achieving this level of control may be quite challenging. On the other hand, precipitation is phenomenon that is time, temperature, and transformation (TTT) dependant. For instance, most of the rapidly solidified materials do not show uneven distribution of particles or excessive precipitation coarsening episodes in the matrix due to limited diffusion range^{85,86}. Therefore, increasing the cooling rate through the precipitation window may prevent uneven distribution of the particles. Therefore, in-depth thermodynamic analysis of the material towards better understanding of the precipitation phenomenon may yield in an AM processing window that can potentially resolve the observed challenges.

METHODS

Materials and conditions

In this study, aluminum alloy AA5083 (Al5MgMn) was deposited on a solution treated and aged Al AA6061 plate. The 5083 alloy is weldable and tolerates thermal gradients that may occur in a processing step⁸⁷. The 6061 alloy was chosen as a substrate, as it is among the most produced high-strength aluminum alloys and it is easily available in the form of plates at a reasonable price range. Our experimental planning required flexibility to remove the substrate material. Therefore, AA6061 was mainly chosen for its availability and price rather than having a substrate with a composition similar to that of the overlaid 5083 alloy. Table 1 shows the chemical compositions of the relevant materials.

Deposition setup and parameters

The WAAM setup consists of an ABB IR2400 robot, carrying a cold metal transfer deposition head connected to the Fronius TPSi-400 power supply unit.

After a few trial-and-error sequences, the material was successfully deposited at 177 A and 15.3 V of arc settings, wire feed rate of 8 m/min and tool traveling speed of 6 mm/s.

Tensile property evaluation and microstructural inspection

Three sets of tensile specimens were prepared from the bulk of the deposited material along the x , y , and z directions (c.f. Fig. 1). The samples were tested in an Instron tensile machine using a conventional extensometer.

For the microstructural investigations, the specimens were taken from the y - z plane (width-height) and the x - y plane with reference to the coordination system shown in Fig. 1.

For the scanning electron microscopy (SEM) inspection of the as-received specimens, three microscopes were used: (a) Hitachi tabletop for EDS mapping and microstructure observations, (b) FEI NOVA NANOSEM 650 ultrahigh vacuum field emission gun scanning electron microscope equipped with an X-Max 50 EDS detector from Oxford Instruments and "Aztec Feature" analysis software, which was used to investigate the chemistry and distribution of the particles, and (c) JEOL JSM 6510 LV SEM for microstructure observations under Backscattered Electron Composition (BEC) mode.

In the "Aztec Feature" method, the SEM images are segmented according to their grayscale value and used as a criterion for identifying a particle in the matrix. Owing to the interaction volume of the electron beam in the SEM, the images may reveal subsurface particles at a different grayscale level and therefore, a threshold value was carefully selected to mask the particles that were not exposed to the surface. The motivation behind excluding subsurface particles was to increase the chemical composition accuracy as subsurface particles show higher content of aluminum. After successful thresholding and segmentation, the exposed particles were identified, and an EDS spectrum was acquired in the geometrical center of each particle. Thus, each spectrum was correlated to a specific particle with reference to the global microscope stage coordination.

Electrochemical testing

The specimens to be tested for corrosion were water jet-cut from the as-fabricated block (c.f. Fig. 1b). Samples from the y - z and x - z surfaces were extracted and tested. Four polished rectangular segments from the y - z plane and four rectangular segments from the x - z plane, each of which belonging to or centered around a different zone of the AM structure (zone a: substrate, zone b: substrate/deposited alloy interface, zone c: interlayer boundary, zone d: within an individual deposition layer). The samples were peripherally mounted in epoxy, leaving an effective surface area of 0.75 (0.3 × 2.5) cm² for zones b, c and 0.84 (0.7 × 1.2) cm² for zones

Table 1. Chemical composition of the alloys based on the supplier certificate.

Element (wt%)	Mg	Mn	Fe	Zn	Cu	Si	Cr	Ti	Others	Al
AA5083	5.0	0.8	0.2	0.15	0.05	0.1	0.05	0.1	<0.15	Rest
AA6061	1.0	0.1	0.3	0.15	0.25	0.5	0.13	0.1	<0.15	Rest

a, d to be exposed to the electrolyte. The samples were subjected to potentiodynamic polarization testing in an aerated 3.5 wt.% NaCl aqueous solution (pH: 7.2). The deposited beads at different distances from the substrate (from the y - z and x - z planes) were also polarized to evaluate the uniformity through the thickness of the deposited block. The samples were electrically connected through spot welding to the Gill AC Weld Potentiostat/Galvanostat. A standard three-electrode cell was employed (reference electrode: Ag/AgCl/sat. KCl, counter electrode: Pt gauze). Following the determination of the rest potential (1 h of immersion in 3.5 wt.% NaCl under open circuit), potentiodynamic polarization started in the potential range of -100 to $+1000$ mV versus the rest potential, at a scan rate of 10 mV/min.

The IR drop due to the electrolyte was expected to be quite small, since the resistivity of 3.5 wt.% NaCl (measured at 25 °C by an electrical conductivity meter) was quite low ($0.019 \text{ m}\Omega \times \text{cm}$). Nevertheless, compensation for IR drop was automatically carried out on the potentiostat by measuring the solution resistance between the working electrode and the reference electrode with an AC signal and then adjusting the output voltage (via the Ohms law) using a PID (proportional-integral-derivative) control algorithm.

Besides anodic potentiodynamic polarization and microstructural observations, the susceptibility of the alloys to various forms of localized corrosion was investigated by cyclic (reverse) polarization. The fundamental concept of this technique is that localized corrosion would occur if the current density of the reverse anodic portion of the polarization curve is higher than the current density of the forward corrosion for the same anodic potential^{67,88}. This behavior is a direct consequence of the more aggressive environment within the propagating pits⁶⁷. Under such conditions, the forward and reverse portions of the scan do not overlap. The hysteresis caused by the current density difference between the forward scan (lower current density) and reverse scan (higher current density) at the same potential was designated as “negative hysteresis” (Further information can be found in⁸³).

Microstructural analysis of the corroded specimens

Cross-sections of the corroded surfaces were ground stepwise by 180, 320, 500, 800, and 1200 grade sandpapers, followed by stepwise polishing by cloth with 6, 3, and 1 μm abrasive media. The prepared cross-sections were examined by SEM-EDS under secondary electron (SE) mode at the JEOL JSM 6510 LV scanning electron microscope equipped with an Oxford Instruments X-Act EDS system.

Corroded surfaces were investigated by an XPS AxisUltraP^{DLDP} XP spectrometer from Kratos Analytical using monochromatic Al K α radiation ($h\nu = 1486.6 \text{ eV}$). Survey spectra were acquired over a $700 \times 300 \mu\text{m}^2$ area with 80 eV pass energy (1.1 eV resolution, as determined by the full width at half maximum of the Ag 3d $_{5/2}$ of metallic silver). The XPS mappings and the extracted detail spectra were acquired over an $800 \times 800 \mu\text{m}^2$ area with 40 eV pass energy (0.8 eV resolution). Charge compensation using low-energy electrons was applied during acquisition in order to ensure good acquisition conditions. The energy scale was referenced based on the position of the C 1s peak from C-C/H bonds in adventitious carbon, set to 284.8 eV binding energy (BE). Quantification was based on the manufacturer’s relative sensitivity factors.

The topography of corroded surfaces was analyzed quantitatively with white light interferometry (WLI) using a Veeco Wyko NT9800.

DATA AVAILABILITY

The raw data required to reproduce these findings can be shared upon request. The processed data required to reproduce these findings are presented completely and the authors do not have any unprocessed data to share beyond the ones presented here.

Received: 3 January 2021; Accepted: 7 May 2021;

Published online: 26 May 2021

REFERENCES

- Shen, C., Pan, Z., Cui, D., Roberts, J. & Li, H. Fabrication of Fe-FeAl functionally graded material using the wire-arc additive manufacturing process. *Metall. Mater. Trans. B.* **47**, 763 (2016).

- Ding, D., Pan, Z., van Duin, S., Li, H. & Shen, C. Fabricating superior NiAl bronze components through wire arc additive manufacturing. *Materials* **9**, 652 (2016).
- Haden, C. et al. Wire and arc additive manufactured steel: tensile and wear properties. *Addit. Manuf.* **16**, 115 (2017).
- Wang, Y. M. et al. Additively manufactured hierarchical stainless steels with high strength and ductility. *Nat. Mater.* **17**, 63 (2018).
- Hack, H. P. *Galvanic Corrosion* Vol. 978. (ASTM International, 1988).
- Miyamoto, Y., Kaysser, W., Rabin, B., Kawasaki, A. & Ford, R. G. *Functionally Graded Materials: Design, Processing and Applications* Vol. 5. (Springer Science & Business Media, 2013).
- Schulz, U., Peters, M., Bach, F.-W. & Tegeder, G. Graded coatings for thermal, wear and corrosion barriers. *Mater. Sci. Eng. A* **362**, 61 (2003).
- Wang, L. et al. Fabrication of a nanocrystalline Ni-Co/CoO functionally graded layer with excellent electrochemical corrosion and tribological performance. *Nanotechnology* **17**, 4614 (2006).
- Ocylok, S., Weisheit, A. & Kelbassa, I. Functionally graded multi-layers by laser cladding for increased wear and corrosion protection. *Phys. Procedia* **5**, 359 (2010).
- Chin, E. S. Army focused research team on functionally graded armor composites. *Mater. Sci. Eng. A* **259**, 155 (1999).
- Jutte, C. V., Stanford, B., Wieseman, C. D. & Moore, J. B. Aeroelastic tailoring of the NASA common research model via novel material and structural configurations. *52nd Aerospace Sciences Meeting*. 13–17 January, National Harbor, MD, USA (2014).
- Atzeni, E. & Salmi, A. Economics of additive manufacturing for end-useable metal parts. *Int. J. Adv. Manuf.* **62**, 1147 (2012).
- Diegel, O., Singamneni, S., Reay, S. & Withell, A. Tools for sustainable product design: additive manufacturing. *Int. J. Sustain. Dev.* **3**, 68 (2010).
- Ruffo, M., Tuck, C. & Hague, R. Cost estimation for rapid manufacturing-laser sintering production for low to medium volumes. *Proc. Inst. Mech. Eng. Pt. B: J. Eng. Manuf.* **220**, 1417 (2006).
- Gibson, I., Rosen, D. W. & Stucker, B. *Additive Manufacturing Technologies*, Vol. 17. (Springer, 2014).
- Brice, C., Shenoy, R., Kral, M. & Buchannan, K. Precipitation behavior of aluminum alloy 2139 fabricated using additive manufacturing. *Mater. Sci. Eng. A* **648**, 9 (2015).
- Cabrini, M. et al. Corrosion resistance of direct metal laser sintering AlSiMg alloy. *Surf. Interface Anal.* **48**, 818 (2016).
- Chua, C. K. & Leong, K. F. *3D Printing and Additive Manufacturing: Principles and Applications (with Companion Media Pack) of Rapid Prototyping*. 4th edn (World Scientific Publishing Company, 2014).
- Ding, Y. et al. Microstructure and mechanical property considerations in additive manufacturing of aluminum alloys. *MRS Bull.* **41**, 745 (2016).
- Zhang, Y., Chen, Y., Li, P. & Male, A. T. Weld deposition-based rapid prototyping: a preliminary study. *J. Mater. Process. Technol.* **135**, 347 (2003).
- Williams, S. W. et al. Wire+ arc additive manufacturing. *Mater. Sci. Technol.* **32**, 641 (2016).
- Szost, B. A. et al. A comparative study of additive manufacturing techniques: residual stress and microstructural analysis of CLAD and WAAM printed Ti–6Al–4V components. *Mater. Des.* **89**, 559 (2016).
- Gu, J. et al. The strengthening effect of inter-layer cold working and post-deposition heat treatment on the additively manufactured Al–6.3 Cu alloy. *Mater. Sci. Eng. A* **651**, 18 (2016).
- Ouyang, J., Wang, H. & Kovacevic, R. Rapid prototyping of 5356-aluminum alloy based on variable polarity gas tungsten arc welding: process control and microstructure. *Mater. Manuf. Process.* **17**, 103 (2002).
- Wu, B. et al. A review of the wire arc additive manufacturing of metals: properties, defects and quality improvement. *J. Manuf. Process.* **35**, 127 (2018).
- Pickin, C. G., Williams, S. W. & Lunt, M. Characterisation of the cold metal transfer (CMT) process and its application for low dilution cladding. *J. Mater. Process. Technol.* **211**, 496 (2011).
- Pickin, C. & Young, K. Evaluation of cold metal transfer (CMT) process for welding aluminium alloy. *Sci. Technol. Weld. Join.* **11**, 583 (2006).
- Almeida, P. & Williams, S. Innovative process model of Ti–6Al–4V additive layer manufacturing using cold metal transfer (CMT). *Proceedings of the twenty-first annual international solid freeform fabrication symposium* (University of Texas at Austin, 2010).
- Gu, J., Cong, B., Ding, J., Williams, S. W. & Zhai, Y. Wire+ arc additive manufacturing of aluminium. *Proceedings of the 25th Annual International Solid Freeform Fabrication Symposium* (University of Texas, 2014).
- Cong, B., Ding, J. & Williams, S. Effect of arc mode in cold metal transfer process on porosity of additively manufactured Al–6.3% Cu alloy. *Int. J. Adv. Manuf. Technol.* **76**, 1593 (2015).
- Cong, B. et al. A comparative study of additively manufactured thin wall and block structure with Al–6.3% Cu alloy using cold metal transfer process. *Appl. Sci.* **7**, 275 (2017).

32. Köhler, M., Fiebig, S., Hensel, J. & Dilger, K. Wire and arc additive manufacturing of aluminum components. *Metals* **9**, 608 (2019).
33. Zhang, C., Li, Y., Gao, M. & Zeng, X. Wire arc additive manufacturing of Al-6Mg alloy using variable polarity cold metal transfer arc as power source. *Mater. Sci. Eng. A*. **711**, 415 (2018).
34. Sander, G. et al. Corrosion of additively manufactured alloys: a review. *Corrosion* **74**, 1318 (2018).
35. Kong, D., Dong, C., Ni, X. & Li, X. Corrosion of metallic materials fabricated by selective laser melting. *NPJ Mater. Degrad.* **3**, 1 (2019).
36. Gharbi, O. et al. Microstructure and corrosion evolution of additively manufactured aluminium alloy AA7075 as a function of ageing. *NPJ Mater. Degrad.* **3**, 40 (2019).
37. Yang, Y. et al. Improved corrosion behavior of ultrafine-grained eutectic Al-12Si alloy produced by selective laser melting. *Mater. Des.* **146**, 239 (2018).
38. Leon, A., Shirizly, A. & Aghion, E. Corrosion behavior of AlSi10Mg alloy produced by additive manufacturing (AM) vs. its counterpart gravity cast alloy. *Metals* **6**, 148 (2016).
39. Fathi, P., Mohammadi, M., Duan, X. & Nasiri, A. M. A comparative study on corrosion and microstructure of direct metal laser sintered AlSi10Mg_200C and die cast A360.1 aluminum. *J. Mater. Process. Technol.* **259**, 1 (2018).
40. Chen, Y. et al. Distinction of microstructure and corrosion evolution of additively manufactured aluminium alloy AA7075 as a function of ageing corrosion resistance of selective laser melted Al-12Si alloy on different planes. *J. Alloy. Compd.* **747**, 648 (2018).
41. Davis, J. R. *Alloying: Understanding the Basics* (ASM International, 2001).
42. Hollingsworth, E. & Hunsicker, H. in *ASM Handbook*. Vol. 13, p. 583 (ASM International, 1987).
43. Kaufman, J. G. *Introduction to Aluminum Alloys and Tempers* (ASM International, 2000).
44. Choi, I.-K., Cho, S.-H., Kim, S.-J., Jo, Y.-S. & Kim, S.-H. Improved corrosion resistance of 5xxx aluminum alloy by homogenization heat treatment. *Coatings* **8**, 39 (2018).
45. Jones, R., Baer, D., Danielson, M. & Vetrano, J. Role of Mg in the stress corrosion cracking of an Al-Mg alloy. *Metall. Mater. Trans. A*. **32**, 1699 (2001).
46. Birbilis, N. & Buchheit, R. G. Electrochemical characteristics of intermetallic phases in aluminum alloys: an experimental survey and discussion. *J. Electrochem. Soc.* **152**, B140 (2005).
47. Yi, G., Sun, B., Poplawsky, J. D., Zhu, Y. & Free, M. L. Investigation of pre-existing particles in Al 5083 alloys. *J. Alloy. Compd.* **740**, 461 (2018).
48. Zhu, Y., Cullen, D. A., Kar, S., Free, M. L. & Allard, L. F. Evaluation of Al 3 Mg 2 precipitates and Mn-rich phase in aluminum-magnesium alloy based on scanning transmission electron microscopy imaging. *Metall. Mater. Trans. A*. **43**, 4933 (2012).
49. Goswami, R., Spanos, G., Pao, P. & Holtz, R. Precipitation behavior of the β phase in Al-5083. *Mater. Sci. Eng. A* **527**, 1089 (2010).
50. Lekatou, A., Pouliou, A., Mavros, H. & Karantzalis, A. Thermal treatment, sliding wear and saline corrosion of Al in situ reinforced with Mg 2 Si and ex situ reinforced with TiC particles. *J. Mater. Eng. Perform.* **27**, 5030 (2018).
51. Georgatis, E. et al. Development of a cast Al-Mg 2 Si-Si in situ composite: microstructure, heat treatment, and mechanical properties. *J. Mater. Eng. Perform.* **22**, 729 (2013).
52. Dinnis, C. M., Taylor, J. A. & Dahle, A. K. As-cast morphology of iron-intermetallics in Al-Si foundry alloys. *Scr. Mater.* **53**, 955 (2005).
53. Shabestari, S. The effect of iron and manganese on the formation of intermetallic compounds in aluminum-silicon alloys. *Mater. Sci. Eng. A*. **383**, 289 (2004).
54. Cao, X. & Campbell, J. The solidification characteristics of Fe-rich intermetallics in Al-11.5 Si-0.4 Mg cast alloys. *Metall. Mater. Trans. A*. **35**, 1425 (2004).
55. Kral, M., Nakashima, P. & Mitchell, D. Electron microscope studies of Al-Fe-Si intermetallics in an Al-11 Pct Si alloy. *Metall. Mater. Trans. A*. **37**, 1987 (2006).
56. Mrówka-Nowotnik, G., Sieniawski, J. & Wierzbńska, M. Intermetallic phase particles in 6082 aluminium alloy. *J. Mater. Process. Technol.* **28**, 69 (2007).
57. Taylor, J. A. Iron-containing intermetallic phases in Al-Si based casting alloys. *Procedia. Mater. Sci.* **1**, 19 (2012).
58. Engler, O. & Miller-Jupp, S. Control of second-phase particles in the Al-Mg-Mn alloy AA 5083. *J. Alloy. Compd.* **689**, 998 (2016).
59. Engler, O., Liu, Z. & Kuhnke, K. Impact of homogenization on particles in the Al-Mg-Mn alloy AA 5454—Experiment and simulation. *J. Alloy. Compd.* **560**, 111 (2013).
60. Lekatou, A. et al. Aluminium reinforced by WC and TiC nanoparticles (ex-situ) and aluminate particles (in-situ): Microstructure, wear and corrosion behaviour. *Mater. Des.* (1980-2015) **65**, 1121 (2015).
61. Lekatou, A., Gkikas, N., Gousia, V., Lentzaris, K. & Karantzalis, A. Effects of in situ intermetallics on the microstructural array and saline corrosion performance of cast Al/WCp composites. *J. Mater. Eng. Perform.* **27**, 5164 (2018).
62. Hatch, J. E. *Aluminum: Properties and Physical Metallurgy* (American Society for Metals, 2000).
63. Zajac, S., Hutchinson, B., Johansson, A. & Gullman, L.-O. Microstructure control and extrudability of Al-Mg-Si alloys microalloyed with manganese. *Mater. Sci. Technol.* **10**, 323 (1994).
64. Kim, S.-J., Kim, S.-K. & Park, J.-C. The corrosion and mechanical properties of Al alloy 5083-H116 in metal inert gas welding based on slow strain rate test. *Surf. Coat. Technol.* **205**, 73 (2010).
65. Rasouli, S., Behnagh, R. A., Dadvand, A. & Saleki-Haselghoubi, N. Improvement in corrosion resistance of 5083 aluminum alloy via friction stir processing. *Proc. Inst. Mech. Eng. Part L: J. Mater.: Des. Appl.* **230**, 142 (2016).
66. Lekatou, A., Sfikas, A., Karantzalis, A. & Sioulas, D. Microstructure and corrosion performance of Al-32% Co alloys. *Corros. Sci.* **63**, 193 (2012).
67. Stansbury, E. E. & Buchanan, R. A. *Fundamentals of Electrochemical Corrosion*. (ASM International, 2000).
68. Jafarzadeh, K., Shahrabi, T. & Hosseini, M. Effect of cathodic polarisation on pitting corrosion of AA5083-H321 aluminium-magnesium alloy in stagnant 3-5% NaCl solution. *Corros. Eng. Sci. Technol.* **44**, 144 (2009).
69. Osorio, W. R. et al. Assessment of electrochemical and mechanical behavior of hot-extruded powders and as-cast samples of Al-Ni alloys. *Int. J. Electrochem. Sci.* **7**, 9946 (2012).
70. Nam, N. et al. Corrosion behaviours of hot-extruded Al-xMg alloys. *J. Mater. Res. Technol.* **8**, 5246 (2019).
71. Seong, J., Frankel, G. & Sridhar, N. Corrosion inhibition of sensitized and solutionized AA5083. *J. Electrochem. Soc.* **162**, C449 (2015).
72. Wang, B., Zhang, L., Su, Y., Xiao, Y. & Liu, J. Corrosion behavior of 5A05 aluminum alloy in NaCl solution. *Acta Metall. Sin. Engl. Lett.* **26**, 581 (2013).
73. Moffat, T., Stafford, G. & Hall, D. Pitting Corrosion of Electrodeposited Aluminum-Manganese Alloys. *J. Electrochem. Soc.* **140**, 2779 (1993).
74. Zhang, J., Zhang, W., Yan, C., Du, K. & Wang, F. Corrosion behaviors of Zn/Al-Mn alloy composite coatings deposited on magnesium alloy AZ31B (Mg-Al-Zn). *Electrochim. Acta* **55**, 560 (2009).
75. Chen, J. et al. The origin of passivity in aluminum-magnesium solid solutions. *Corros. Sci.* **173**, 108749 (2020).
76. Foley, R. Localized corrosion of aluminum alloys—a review. *Corrosion* **42**, 277 (1986).
77. Szklarska-Smialowska, Z. Pitting corrosion of aluminum. *Corros. Sci.* **41**, 1743 (1999).
78. Macdonald, D. D. The point defect model for the passive state. *J. Electrochem. Soc.* **139**, 3434 (1992).
79. Serdechnova, M., Volovitch, P., Brisset, F. & Ogle, K. On the cathodic dissolution of Al and Al alloys. *Electrochim. Acta* **124**, 9 (2014).
80. Birbilis, N. & Buchheit, R. Investigation and discussion of characteristics for intermetallic phases common to aluminum alloys as a function of solution pH. *J. Electrochem. Soc.* **155**, 117 (2008).
81. Pourbaix, M. Applications of electrochemistry in corrosion science and in practice. *Corros. Sci.* **14**, 25 (1974).
82. Frankel, G. Pitting corrosion of metals: a review of the critical factors. *J. Electrochem. Soc.* **145**, 2186 (1998).
83. Lekatou, A., Sioulas, D., Karantzalis, A. & Grimanellis, D. A comparative study on the microstructure and surface property evaluation of coatings produced from nanostructured and conventional WC-Co powders HVOF-sprayed on Al7075. *Surf. Coat. Technol.* **276**, 539 (2015).
84. Marola, S. et al. A comparison of Selective Laser Melting with bulk rapid solidification of AlSi10Mg alloy. *J. Alloy. Compd.* **742**, 271 (2018).
85. Prashanth, K. G. et al. Microstructure and mechanical properties of Al-12Si produced by selective laser melting: effect of heat treatment. *Mater. Sci. Eng. A*. **590**, 153 (2014).
86. Lavernia, E., Rai, G. & Grant, N. Rapid solidification processing of 7xxx aluminium alloys: a review. *Mater. Sci. Eng.* **79**, 211 (1986).
87. Johansen, A. *Microstructures and Properties of Aluminium-magnesium Alloys with Additions of Manganese, Zirconium and Scandium*. The Norwegian University of Science and Technology (NTNU) (2000).
88. Revie, R. W. *Uhlig's Corrosion Handbook*. Vol. 51 (John Wiley & Sons, 2011).

ACKNOWLEDGEMENTS

The fund of this work was provided by the AddMan-Al project under the Hydrosfond funding scheme. The authors would like to acknowledge the member of the Hydrosfond board for their support. Dr. M'hamdi is greatly acknowledged for his positive advice throughout the work. Mr. Morten H. Danielsen has processed the deposited materials and the authors appreciate the quality of the material he processed.

AUTHOR CONTRIBUTIONS

A.S.A.: conceptualization, additive manufacturing of the materials, mechanical tests and drafting of the article, and project lead. A.L.: corrosion tests, microstructural analysis and drafting of the article. M.F.S.: XPS studies, interpretation of the results and drafting of the article. J.S.G.: SEM studies, particle characterizations and interpretation of the results. N.T.: corrosion tests and interpretation of the corrosion results. S.D.: conceptualization and drafting of the article.

COMPETING INTERESTS

The authors declare no competing interests.

ADDITIONAL INFORMATION

Correspondence and requests for materials should be addressed to A.S.A.

Reprints and permission information is available at <http://www.nature.com/reprints>

Publisher's note Springer Nature remains neutral with regard to jurisdictional claims in published maps and institutional affiliations.



Open Access This article is licensed under a Creative Commons Attribution 4.0 International License, which permits use, sharing, adaptation, distribution and reproduction in any medium or format, as long as you give appropriate credit to the original author(s) and the source, provide a link to the Creative Commons license, and indicate if changes were made. The images or other third party material in this article are included in the article's Creative Commons license, unless indicated otherwise in a credit line to the material. If material is not included in the article's Creative Commons license and your intended use is not permitted by statutory regulation or exceeds the permitted use, you will need to obtain permission directly from the copyright holder. To view a copy of this license, visit <http://creativecommons.org/licenses/by/4.0/>.

© The Author(s) 2021